Structural basis of the differential binding of engineered knottins 2.5F and 2.5D to integrins αVβ3 and α5β1

Johannes F. Van Agthoven [1,2,3], Hengameh Shams [4], Frank V. Cochran [5], Jose´ L. Alonso [1,2,3], James R. Kintzing [5], Kiavash Garakani [4], Jian-Ping Xiong [1,2,3], Mohammad R. K. Mofrad [4], Jennifer R. Cochran [5] and M. Amin Arnaout [1,2,3*]

[1]Leukocyte Biology and Inflammation Program, [2]Structural Biology Program, [3]Division of Nephrology/Department of Medicine, Massachusetts General Hospital and Harvard Medical School, Charlestown, MA, 02129, USA; [4] Departments of Bioengineering and Mechanical Engineering, University of California, Berkeley, CA, 94720, USA. [5] Departments of Bioengineering and Chemical Engineering, Stanford University, Stanford, CA, 94305, USA.

* Correspondence: EM: aarnaout1@mgh.harvard.edu

Keywords : Integrins; Receptors/Structure-Function; Protein crystallography; NMR; Molecular dynamics; Cancer therapy

Abstract
Integrins αVβ3 and α5β1 play critical roles in tumor survival, invasion, metastasis, and angiogenesis and are validated targets for cancer therapy and molecular imaging. Increasing evidence suggests that targeting both integrins simultaneously with antagonists is more effective in cancer therapy because of concerns about resistance and paradoxical promotion of tumor growth with use of agents highly selective for a single integrin. Engineered Arg-Gly-Asp (RGD)-containing 3.5 kDa cysteine-knot proteins (knottins 2.5F and 2.5D) are attractive drug candidates due to their exceptional structural stability and high affinity binding to certain integrins. 2.5F binds both αVβ3 and α5β1, whereas 2.5D is αVβ3-selective. To elucidate the structural basis of integrin selection, we determined the structures of 2.5F and 2.5D both as apo-proteins and in complex with αVβ3. These data, combined with MD simulations and mutational studies, revealed a critical role of two αVβ3-specific residues in the vicinity of the *m*etal *i*on *d*ependent *a*dhesion *s*ite (MIDAS) in promoting an αVβ3-induced fit of 2.5D. In contrast, conformational selection accounted for the specificity of 2.5F to both integrins. These data provide new insights into the structural basis of integrin-ligand binding specificity, and could help in development of integrin-targeted therapeutics.

Introduction

Heterodimeric α/β integrins comprise a large family of divalent cation-dependent adhesion receptors that mediate cell-cell and cell-matrix interactions, which underlie their essential roles in normal metazoan physiology but also in contributing to many diseases including pathologic thrombosis, inflammation, autoimmunity, osteoporosis and cancer (Raab-Westphal et al., 2017). In response to cell-activating stimuli, intracellular signals are generated that rapidly convert integrins into a ligand-binding state, a process termed inside-out activation (Arnaout et al., 2007). Physiologic ligands, prototyped by the Arg-Gly-Asp (RGD) sequence motif, then bind the integrin head (formed of the α-subunit propeller and β-subunit βA domains) (Xiong et al., 2002). A carboxylate group of the ligand Asp makes an electrostatic contact with a Mg^{2+} ion coordinated at MIDAS of the βA domain, and the ligand Arg inserts into a pocket in the α-subunit propeller. Ligand binding induces tertiary changes in βA that are converted to quaternary changes in the ectodomain, thus forging links of the integrin cytoplasmic tails with the actin cytoskeleton to regulate cell function, a process termed outside-in signaling (Friedland et al., 2009).

Therapeutic targeting of integrins has generally focused on development of peptides or small molecules that primarily target a single integrin (Kapp et al., 2017), an approach that has been effective in platelets, where integrin αIIbβ3 is most abundant (Coller and Shattil, 2008). However, in other cell types expressing multiple integrins, high selectivity for a single integrin may promote upregulation of another integrin sharing the same ligand, leading to reduced effectiveness, drug resistance, or even paradoxical effects. This scenario may be particularly relevant in cancer cells, where primary targeting of αVβ3 integrin with cilengitide failed to prolong survival of patients with glioblastoma (Mason, 2015), likely related to unfavorable pharmacokinetics, agonist-like behavior (Reynolds et al., 2009), enhanced α5β1-mediated cell migration (Caswell et al., 2008; Christoforides et al., 2012), or both. Recent studies also showed superiority of targeting αVβ3 plus α5β1 as compared to αVβ3 alone in noninvasive *in vivo* imaging of brain cancer in mice (Moore et al., 2013).

The engineered knottin miniproteins 2.5D and 2.5F bind with high affinity to αVβ3 (2.5D) or to both αVβ3 and α5β1 (2.5F) (Kimura et al., 2009a). Knottins 2.5D and 2.5F only differ in four residues: two on either side of the RGD motif, flanked by prolines (Fig. 1A). To elucidate the structural basis for integrin selectivity, we determined the solution structures of 2.5D and 2.5F and their crystal structures in complex with αVβ3. The results of these studies are the subject of this report.

Results

Integrin binding to 2.5D and 2.5F. We measured binding of 2.5D-Fc or 2.5F-Fc fusion proteins to K562 cells stably expressing recombinant αVβ3 (αVβ3-K562) and to K562 cells, which constitutively express α5β1 integrin. 2.5D bound to αVβ3-K562 cells with high affinity (Fig. 1B, D), but bound minimally to K562 cells (Fig. 1B), whereas 2.5F bound both cells with high affinity (Fig. 1C, D). Both 2.5D and 2.5F bound to U87MG glioblastoma cells, which express high levels of αVβ3 and α5β1 integrins (Dumont et al., 2009).

NMR structures of 2.5D and 2.5F. To begin to elucidate the structural basis for selectivity of knottin/integrin binding, we first determined the solution structures of 2.5D and 2.5F by NMR (Table S1). As expected, both knottins assumed the same compact structure held together by three disulfide bonds, typical of the cysteine inhibitor family (Fig. 2A, B). However, structure of the engineered RGD-containing loop flanked by prolines 3 and 11 was drastically different in the two knottins (Fig. 2A, B). In 2.5D, this loop maintains a nearly single packed conformation (Fig. 2A, C, D), but is highly flexible in 2.5F (Fig. 2B-D).

X-ray structures of integrin-bound 2.5D and 2.5F. Knottins 2.5D and 2.5F were each soaked into preformed αVβ3 ectodomain crystals in presence of 1 mM Mn^{2+} and the crystal structure of the respective complex was determined as previously described (Van Agthoven et al., 2014; Xiong et al., 2002). Simulated annealing composite omit maps showed clear ligand density, and allowed complete tracing of the knottin macromolecule (Fig. 3A, B and Table S2) with Real Space Cross Correlations (RSCCs) for RGD in both knottins of 0.93-0.97, suggesting almost full occupancy of the ligand. The RGD motif of each ligand inserted into the crevice between the propeller and βA domains and contacted both in an identical manner (Fig. 3C, D). The guanidine of Arg^{6} of each knottin contacts αV-Asp^{218} of the propeller, with a carboxylate from Asp^{8} contacting the MIDAS Mn^{2+}. In the 2.5D/αVβ3 structure, 2.5D residues Gln^{4}, Ala^{10}, Pro^{11}, Pro^{28}, Asn^{29} and Phe^{31} form additional van der Waals contacts with βA (Fig. 3E). In the 2.5F/αVβ3 structure, 2.5F-Arg^{4} hydrogen bonds with βA-Asn^{313} and contacts the ADMIDAS metal ion indirectly through a chloride ion (Fig. 3D). Other interactions include van der Waals contacts of 2.5F residue Pro^{10}, Pro^{11}, and Phe^{31} with βA (Fig. 3F). These interactions, which bury a surface area of 654.6 $Å^2$ for 2.5F/αVβ3 and 606.2 $Å^2$ for 2.5D/αVβ3 structures account for the high affinity binding of each ligand to αVβ3.

As with binding of the natural ligand FN10 or the partial agonist cilengitide to αVβ3 (Van Agthoven et al., 2014; Xiong et al., 2002), binding of 2.5D or 2.5F induced a 3.7Å displacement of the α_1 helix of the βA domain towards the MIDAS Mn^{2+} and the restructuring of the F/α7 loop (Supplemental Fig. 1A), indicating that both knottins are partial agonists. The shape of the CD

loop of the βTD in both knottin/integrin structures was also comparable to the one published for αVβ3-wtFN10 (Van Agthoven et al., 2014) (Supplemental Fig. 1 B-D). However, whereas the crystal structure of the pure antagonist hFN10 bound to αVβ3 showed a h-bond between β_3-Glu^{319} of βA and β3-Ser^{674} of βTD and a visible glycan at Asn^{711}, both features were absent in the αVβ3-2.5F and αVβ3-2.5D structures (Supplemental Fig. 1 B-D).

Conformations of the RGD-containing loops of 2.5D and 2.5F bound to $\alpha_V\beta_3$. In contrast to the major differences in conformation of the RGD-containing loops of 2.5D and 2.5F seen in the NMR structures (Fig. 2), the two loops were largely superposable in the integrin-bound state (Fig. 4A), with a root mean square deviation (r.m.s.d.) of 0.62±0.27Å^2 (mean±sd). Superposing the crystal structures of the integrin-bound loops on the respective NMR structure of the lowest energy state showed dramatic differences in the RGD-containing loop of 2.5D (Fig. 4B). The r.m.s.d. of this loop in 2.5D between the integrin-bound and solution states is 3.52 ±1.01Å^2, which is significantly higher than its narrow r.m.s.d. in solution (0.67±0.22 Å^2, Figure 2D). The apo-protein state is stabilized by a 4-residue type I β-turn spanning Arg^6 to Trp^9, with hydrogen bonds from the carbonyl oxygen of Arg^6 and Gly^7 to the amide nitrogen of Trp^9 and Asp^8, respectively, and maintains a distance of ~6.4 Å between the β carbons of Arg^6 and Asp^8 ($C^{RD}_{\beta-\beta}$)(Fig. 4C). When 2.5D is bound to αVβ3, the β-turn unfolds, with Trp^9 moving from the solvent-exposed state to form an internal van der Waals bond with Gly^5 (Fig. 4D), thus extending the $C^{RD}_{\beta-\beta}$ distance to 9Å (Fig. 4E). In contrast, the r.m.s.d. of the RGD-containing loop of 2.5F between the bound and solution structure is 3.13±1.64Å^2, comparable to its r.m.s.d. in solution (2.76±1.0 Å^2) (Fig. 4F), with the $C^{RD}_{\beta-\beta}$ varying from 4.1Å to 8.8 Å (Fig. 4G), approaching the 9.1Å $C^{RD}_{\beta-\beta}$ found in αVβ3/2.5F (Fig. 4H) or RGD-bound α5β1 ($C^{RD}_{\beta-\beta}$=8.8Å) (Fig. 4I).

MD simulations of 2.5D and 2.5F binding to $\alpha_V\beta_3$ and $\alpha_5\beta_1$. The low energy of interaction between 2.5D-Trp^9 and 2.5D-Gly^5 suggests that surrounding residues in the binding pocket of αVβ3 are involved in the conformational switch of 2.5D-Trp^9 from the solvent to the buried state. We therefore used MD simulation to characterize the early stage of binding of 2.5D to αVβ3 vs. α5β1. The lowest energy NMR structures of 2.5D and 2.5F were docked onto the αVβ3 and α5β1 crystal structures, resulting in four protein complexes. In each complex, the knottin was moved 9Å away from the integrin surface allowing several water layers to form between the two before simulation was initiated. Over a 500-ns run, 2.5D bound to αVβ3 (164±37 kcal/mole), but diffused away from α5β1 after a few nanoseconds of interaction (7±19 kcal/mole), whereas 2.5F associated effectively with both αVβ3 (135±37 kcal/mole) and α5β1 (81±51 kcal/mole) (Fig. 5A, B), recapitulating the cell-based data (Fig. 1 B-D). Over the course of the αVβ3/2.5D simulation, 2.5D-Trp^9 first formed an S-π bond with β3-Met^{180} 0.38 ns after start of simulation, which was reinforced at 0.96 ns via an electrostatic interaction between 2.5D-Asp^8 and β3-Arg^{214} (Fig. 5C, D).

Binding of 2.5D and 2.5F to native and mutant cellular αVβ3. To assess the contribution of these early contacts on the binding energy of 2.5D to αVβ3, we made two substitutions in αVβ3 where β_3-Met^{180} was changed to alanine (β_3-Met^{180} has no homolog in β1) and β3-Arg^{214} replaced by glycine (the equivalent residue in β_1). MD simulations showed that the Met^{180}/Arg^{214}-Ala-Gly α αVβ3 mutant (αVβ3**) sustained a significant loss in binding energy (25±19%) to 2.5D, but maintained the energy of interaction (111±19%) with 2.5F (Fig. 6A, B). To validate the MD data, we quantified the binding of Alexa-647-labeled 2.5F and 2.5D to wild-

type αVβ3and αVβ3**, each transiently expressed in HEK293 cells. The double mutation reduced surface expression of $\alpha_v\beta_3^{**}$ by ~50% compared to wild-type αVβ3 (Fig. 6C). When binding of each labeled ligand to the integrin was corrected for the degree of expression, binding of 2.5F to αVβ3** was minimally affected (85±9% of binding to wt- αVβ3, Fig. 6D), but binding of 2.5D to αVβ3** was markedly reduced (28±1% of binding to wt- αVβ3) (Fig. 6E).

Discussion

We investigated the structural basis for the differential binding of the two engineered knottins 2.5D and 2.5F to integrins αVβ3 and α5β1. These studies show that specific recognition of αVβ3 by 2.5D requires high structural plasticity of the RGD-containing loop, which becomes apparent from the major conformational changes in loop backbone observed when the structure of the apo-protein and αVβ3/2.5D complex are compared. These comparisons also reveal a pronounced induced fit binding mechanism upon complex formation with αVβ3, which in addition to its high structural plasticity resemble the well-known interactions between antibodies and antigens (Wilson and Stanfield, 1994). These features were not observed in binding of 2.5F to αVβ3, where the RGD-containing loop of the apo-protein is very flexible, with some conformers having a $C_{\beta-\beta}^{RD}$ distance comparable to that found in the αVβ3-bound state, suggesting that 2.5F binds αVβ3 by conformation selection.

MD simulations elucidated the structural basis of the induced fit that underlies binding of 2.5D to αVβ3. The RGD-containing loop in the apo-protein is stabilized by a Type I β-turn, yielding a $C_{\beta-\beta}^{RD}$ distance of ~6.4Å, which extends to the optimal 9Å distance as a result of conformational switch of 2.5D-Trp^9 from a solvent to a buried state. The conformational switch in 2.5D-Trp^9 is driven by an early contact with β3-Met^{180} followed by one with β3-Arg^{214} and later influenced by the surrounding hydrophilic environment (β_3-Tyr^{166}, β3-Arg^{214}), as 2.5D-Asp^8 coordinates the metal ion at MIDAS. Substitution of β3-Met^{180} to Ala and β3-Arg^{214} to Gly (as in β_1) resulted in a major loss in binding energy of 2.5D to αVβ3. This was confirmed in assessing knottin binding to HEK293 transiently expressing wild-type αVβ3 or αVβ3**. Since α5β1 lacks the equivalent Met and Arg residues, the induced fit mechanism cannot proceed, accounting for the lack of binding of 2.5D to α5β1. The $C_{\beta-\beta}^{RD}$ distance offered by some conformers of the flexible RGD-containing loop in 2.5F also account for its high affinity binding to α5β1.

The differences between 2.5F and 2.5D in adapting to the ligand-binding pocket in α5β1 likely relates to the RGD flanking residues of each ligand. Notably, 2.5F harbors two more prolines Pro^5 and Pro^{10} in the RGD-containing loop (PRP*RGD*NPPLT) when compared to that in 2.5D (PQG*RGD*WAPTS)(Fig. 1A)(Kimura et al., 2009b). These prolines likely introduce local rigidity through their pyrrolidine ring, limiting the backbone dihedral angle to ~ 90°, thus restraining the RGD-containing loop from adopting a β-turn fold, as in 2.5D. Previous studies on cyclopeptides show that stability of the RGD loop favors high affinity binding to integrins as it decreases the entropy term of the Gibbs free energy. However, this study shows that it also limits the ability of the peptide, or in this case the miniprotein, to bind various types of RGD pockets in integrins. The critical proline residues in the RGD-containing loop of 2.5F achieves this fine equilibrium between stability and flexibility enabling focused motional freedom (Krieger et al., 2005; Pabon and Camacho, 2017), where the RGD motif is flexible enough to bind various types

of RGD pockets by conformational selection without excessive entropic contribution, which would hamper high affinity binding.

Eight of the 24 known mammalian integrins, including αVβ3 and α5β1, bind to an RGD motif present in a host of natural ligands (Takada et al., 2007). High affinity peptidomimetics or RGD-like small molecules targeting single integrins have been developed. However, most of these ligand-mimetic small molecule antagonists continue to have residual but significant affinity to other RGD-binding integrins as well, and the selectivity of newer versions have not yet been fully explored in cell-based systems and at the high concentrations likely required *in vivo* (Kapp et al., 2017). Given the ability of cancer cells to utilize αVβ3 and α5β1 integrins for growth and metastasis, small molecules with multispecificity have been developed for potential applications in cancer therapy (Hatley et al., 2018; Sheldrake and Patterson, 2014). Despite these successes, development of multifunctional small molecule integrin antagonists that maintain high affinity and suitable pharmacokinetic properties remains a challenge (Nero et al., 2014). The engineered knottin miniproteins 2.5D and 2.5F have a number of advantages over small molecules and short peptides including exceptional structural stability, high affinity, and multispecificity to a number of tumor-associated integrins (Kimura et al., 2009b; Kwan et al., 2017). Their amenability to large-scale synthesis or recombinant expression as fusion proteins in *E. coli* or yeast provides a manufacturing advantage over monoclonal antibodies. These features highlight knottins as promising candidates to bridge a gap between small molecule drugs and monoclonal antibodies.

Methods

Peptide Synthesis EETI-II peptides were prepared as previously described in detail (Kimura et al., 2009b). Briefly, the linear peptide sequences were made by solid-phase peptide synthesis on a CS Bio (Menlo Park, CA) instrument using standard 9-fluorenylmethyloxycarbonyl chemistry. Knottin peptides were folded by promoting disulfide bond formation in oxidizing buffer at room temperature with gentle rocking overnight. Folded EETI-II peptides were purified by reversed-phase HPLC, where they appeared as a sharp peak with a shorter retention time than unfolded or misfolded precursors. The molecular masses of folded EETI-II were determined by matrix-assisted laser desorption/ionization time-of-flight (MALDI-TOF) mass spectrometry (Stanford Protein and Nucleic Acid Facility). Folded knottin peptides (2 mg/mL) were incubated with an amine-reactive succinimidyl ester derivative of Alexa Fluor 647 carboxylic acid in 0.1 M Hepes, pH 8.0, at a 5:1 dye/peptide molar ratio for 1 h at room temperature and then at 4 °C overnight. The free dye was removed by dialysis and buffer exchange into phosphate buffered saline (PBS).

Reagents and antibodies Restriction and modification enzymes were obtained from New England BioLabs Inc. (Beverly, MA). Cell culture reagents were purchased from Invitrogen Corp (San Diego, CA) or Fisher Scientific (Hampton, NH). PBS was from Invitrogen/Boston Biolabs. Integrin binding buffer (IBB) was composed of 25 mM Tris pH 7.4, 150 mM NaCl, 2 mM $CaCl_2$, 1 mM $MgCl_2$, 1 mM $MnCl_2$, and 0.1% bovine serum albumin (BSA).

Plasmids, mutagenesis, protein expression and purification. The human $\alpha_V\beta_3$ ectodomain was expressed in insect cells and purified as described (Mehta et al., 1998). The genetic sequence for knottins 2.5F or 2.5D was fused to the fragment crystallizable (Fc) region of mouse IgG in the pADD2 shuttle vector. The knottin Fc fusion proteins were expressed in human embryonic kidney (HEK293) cells following the manufacturer's protocols in the FreeStyle MAX 293 Expression System (Invitrogen). Secreted knottin Fc fusion proteins were purified using Protein A Sepharose (Sigma) followed by size exclusion chromatography (Superdex 75 column; GE Life Sciences). Purified 2.5F–Fc and 2.5D-Fc were bivalent homo-dimers of the expected molecular weight of ~60 kDa.

Cell lines, cell culture, and transfection. U87MG glioblastoma cells, K562 leukemia cells, and HEK293T embryonic kidney cells were obtained from American Type Culture Collection (Manassas, VA); integrin-transfected K562 cells (Blystone et al., 1994) were provided by Scott Blystone (SUNY Upstate Medical University). U87MG cells were cultured in Dulbecco's Modified Eagle Medium (DMEM) supplemented with 10% Fetal Bovine Serum (FBS) and 1% penicillin-streptomycin (P/S). K562 cells were grown in liquid culture in Iscove's Modified Dulbecco's Medium (IMDM) supplemented with 10% FBS and 1% P/S. HEK293T cells were cultured in DMEM supplemented with 10% FCS, 2 mM l-glutamine, 1 mM sodium pyruvate, penicillin, and streptomycin, and were transiently co-transfected with pcDNA3 plasmids encoding full-length wild-type αVβ3, αVβ3** (αVβ3 β3-M180A and β3-R214G) using Lipofectamine 2000 reagent (Invitrogen) according to the manufacturer's protocol.

Binding assays. 2.5D-Fc and 2.5F-Fc fusions were labeled with the succinimidyl ester derivative of Alexa Fluor 488 (Invitrogen) according to the manufacturer's protocol. Free dye was removed by dialysis and buffer exchange into PBS. U87MG cells were detached using Enzyme-Free Cell Dissociation Buffer (Gibco); K562 cells were grown in suspension. For each cell type, 4×10^4

cells were incubated with varying concentrations (0.01 – 500 nM) of Alexa Fluor 488 labeled 2.5D- or 2.5F-Fc fusion proteins in IBB for 3 h at 4 °C, to minimize internalization. Cells were pelleted and washed twice with 800 µL of PBSA (phosphate buffered saline containing 0.1% bovine serum albumin) and the fluorescence of remaining surface-bound protein was measured by flow cytometry using a Guava EasyCyte 8HT instrument (EMD Millipore). Resulting data were evaluated using FlowJo software (TreeStar Inc.) and equilibrium dissociation constants (Kd) were determined using Prism software (GraphPad). Error bars represent the standard deviation of experiments performed in triplicate.

Wild type αVβ3 and mutated αVβ3** transiently transfected HEK293T cells were gently trypsinized and washed in DPBS buffer. Cells were re-suspended in complete culture medium, incubated for one hour at 37˚C and subsequently washed in 1 mM Ca^{2+}/Mg^{2+}, 0.1% bovine serum albumin-supplemented Hepes buffered saline pH 7.4 (binding buffer). 5×10^6 cells were incubated with Alexa647-labeled 2.5F or 2.5D (50 nM) in binding buffer for 30 min, at 25 °C then washed, re-suspended, fixed in 1% paraformaldehyde and analyzed by flow cytometry in a LSRII flow cytometer (BD). Anti-$\alpha_V\beta_3$ antibody LM609 (20 µg/ml) was used to normalize $\alpha_V\beta_3$ cell surface expression in a separate set of tubes. Transfected HEK293T cells were stained with LM609 for 30 min at 4˚C. After washing the excess antibody, APC-labeled goat anti-mouse Fc-specific antibody (10 µg/ml) was added for 30 min at 4°C, and the stained cells were washed, fixed and expression analyzed by flow cytometry as described above. Alexa-647 labeled knottin 2.5F or 2.5D binding to αVβ3 and αVβ3** was measured in mean fluorescence intensity (MFI) units, normalized according to LM609 binding and expressed as percentage of 2.5F or 2.5D binding to αVβ3. The results presented are the average of three independent experiments.

NMR A codon-optimized DNA sequence was prepared by assembly PCR and cloned into the pET-32 vector to express a protein product in *E. coli* containing a thioredoxin and His-tag fusion protein separated by a TEV protease site. Uniform ^{15}N- and ^{13}C-labeling was achieved by IPTG-induced expression in BL21-DE3 cells in M9 minimal media containing $^{15}NH_4Cl$ and ^{13}C-glucose. Cell lysis was followed by initial purification by His-tag capture with Ni-NTA. The thioredoxin fusion protein portion was removed with TEV protease to provide the exact 33-residue peptide sequence. Disulfide bond formation to fold the peptides was performed using the previously reported redox buffer (Kimura et al., 2009b). Final purification by RP-HPLC and characterization by ESI mass spectrometry confirmed folded engineered EETI-II peptides. NMR samples were prepared using sodium phosphate buffer, pH 6 containing 10% D_2O. Standard multidimensional NMR datasets were acquired for backbone and side chain resonance assignments, along with ^{13}C (aliphatic and aromatic) and ^{15}N 3D-NOESY datasets for NOE-derived distance restraints. Dihedral angle restraints were derived from backbone assignments using TALOS+. 3D structure calculations were performed using the CYANA automated NOE assignment and simulated annealing algorithms. Initial structures calculated using standard automated NOE assignments led to convergence of 20 lowest energy structures, which were consistent with the expected EETI-II disulfide pattern. Further improved 3D structures were calculated by including disulfide bond restraints and hydrogen bond restraints determined by cross-hydrogen bond scalar couplings identified from long-range HNCO datasets. Final structures were refined by restrained molecular dynamics in explicit solvent using the YASARA package.

Crystallography, structure determination and refinement. The αVβ3 ectodomain was crystallized at 4 °C by vapor diffusion using the hanging drop method as previously described (Xiong et al., 2009; Xiong et al., 2001; Xiong et al., 2002). EETI-II 2.5F or 2.D (5 mM) was soaked into $\alpha_v\beta_3$ crystals in the crystallization well solution containing 1 mM Mn^{2+} for 2–3 weeks. Crystals were harvested in 12% PEG 3500 (polyethylene glycol, molecular weight 3500) in 100 mM sodium acetate, pH 4.5, 800 mM NaCl plus 2 mM Mn^{2+} and knottin 2.5F or 2.5D (at 5 mM), cryoprotected by the addition of glycerol in 2% increments up to a 24% final concentration and then flash frozen in liquid nitrogen. Diffraction data from cryo-cooled crystals were collected on the ID19 beamline fitted with a CCD detector at the APS Facility (Chicago, IL). Data were indexed, integrated and scaled with the HKL2000 (Otwinowski and Minor, 1997) program. Phases were determined by molecular replacement using PHASER (McCoy et al., 2007), with the structures $\alpha_V\beta_3$ ectodomain (PDB ID 4MMX). Resulting model was subsequently refined by rigid body and simulated annealing using Phenix 1.10.1. The structure EETI-II was traced by the extra density using PDB 2IT7 and introducing the engineered mutations using Coot (Emsley and Cowtan, 2004). The resulting models were refined with the 1.10.1 version of Phenix (Adams et al., 2010) using simulated annealing, TLS, positional and individual temperature-factor refinement and default restrains. Several cycles of refinement and model building using Coot were applied to refine the structures of αVβ3-2.5D, αVβ3-2.5F (Supplemental Table 1), with automatic optimization of X-ray and stereochemistry and additional Ramachandran restrains in the last cycles. The Ramachandran statistics were as follows: $\alpha_V\beta_3$–2.5D structure, 89.8% in the most favored regions, 9.5% in additional allowed regions and 0.7% outliers; αVβ3/2.5F structure, 91.3% in the most favored regions, 8.4% in additional allowed regions and 0.3% outliers. A-weighted 2*Fo-Fc* electron density map was generated from the final models and structure factors using Phenix. All structural illustrations were prepared with the PyMol software (Schrödinger).

Docking and Initial Configurations. The NMR structures of 2.5F (PDB: 6MM4) and 2.5D (PDB ID: 2M7T) were docked onto the crystal structures of the integrin αVβ3 (PDB ID: 4MMZ) and α5β1 (PDB ID: 4WJK) headpieces using the expert interface of the HADDOCK webserver. Four HADDOCK docking runs, between integrin α5β1 and 2.5D, integrin α5β1 and 2.5F, integrin αVβ3 and 2.5D, and integrin αVβ3 and 2.5F were performed. As docking inputs, the RGD sequence was specified as the active site of 2.5D and 2.5F. Residues α5-Glu^{221}, α5-Asp^{227}, and Mg^{2+} ion at the MIDAS site were specified as the active site of integrin α5β1, while residues αV-Asp^{150}, αV-D^{218}, and the MIDAS Mn^{2+} ion, were specified as the active site of integrin αVβ3. To preserve the ion coordination of the MIDAS, ADMIDAS, and LIMBS ions during the docking run, unambiguous distance restraints between the coordinating groups and the MIDAS, ADMIDAS, and LIMBS ions were fed into HADDOCK. Furthermore, integrins αVβ3 and α5β1 were specified as non-flexible in HADDOCK to prevent integrin backbone movement during docking. The RGD sequence of the knottins were specified as semi-flexible, while the non-RGD sequence was specified as non-flexible. Upon completion of the docking runs, the top solution from each generated cluster was analyzed. The best solution was then selected from these solutions based on maximal engagement of the specified active site residues.

Molecular Dynamics Simulations To simulate the interaction of 2.5D and 2.5F with integrins αVβ3 and α5β1, we performed Molecular Dynamics simulations using the top solution from each of the four HADDOCK structures. To setup the separated simulations, the axis between the

center of mass of the integrin βA domain and the knottin variants was determined in the four HADDOCK complexes. Knottin was then separated from the integrin by 9Å along this axis, allowing water molecules to populate the space in between the knottin and the integrin upon solvation of the structure. We also performed equilibration simulations on the available crystal structures of αVβ3 in complex with 2.5D and 2.5F to be used as references. All structures were solvated and then ionized at a combined KCl concentration of 0.15 M. Structures were subsequently minimized for 100,000 steps and equilibrated for 0.5 ns using the NAMD molecular dynamics package (Phillips et al., 2005) and CHARMM27 force field (Brooks et al., 2009). Upon minimization, each of the four generated complexes ran for 500 ns. All simulations ran at an initial temperature of 310 K using the Nose-Hoover thermostat, and pressure was maintained at 1 atm using the Langevin piston. All equilibration and production run simulations were performed using a time step of 2 fs. Electrostatics of the system were determined using the Particle mesh Ewald (PME) method. Van der Waals (VDW) interactions were modeled using a switching function to smoothly reduce the VDW force to zero at the cutoff distance of 1.2 nm. Simulations were then analyzed using Visual Molecular Dynamics (VMD) (Humphrey et al., 1996).

Acknowledgements. This work was supported by NIH grants DK088327 and DK48549 (to MAA), DK101628 (to JVA), from the National Institutes of Diabetes, Digestive and Kidney diseases (NIDDK) of the National Institutes of Health; the Stanford Bio-X Interdisciplinary Initiatives Program, the Stanford Cancer Institute and the Stanford Maternal & Child Health Research Institute (JRC); National Science Foundation (NSF) grant CBET-0829205 (to MRKM). This work used resources of the Extreme Science and Engineering Discovery Environment (XSEDE) awarded to MRKM, which is supported by the National Science Foundation (NSF) (grant ACI-1053575). JRK was supported by a National Science Foundation Graduate Research Fellowship and an ARCS Scholar Award.

Author contributions. JVA, JLA, JRK and JRC designed and performed the ligand-binding studies. FVC performed the NMR studies. JVA collected the x-ray diffraction data and refined the crystal structures with JPX. HS, KG and MRKM generated the molecular dynamic simulation data. All authors interpreted the data. MAA conceived and oversaw the project and wrote the manuscript with input from all authors.

Competing financial interests. The authors declare no competing financial interests.

Data availability. The authors declare that all data supporting the findings of this study are available within the paper.

References

Adams, P.D., Afonine, P.V., Bunkoczi, G., Chen, V.B., Davis, I.W., Echols, N., Headd, J.J., Hung, L.W., Kapral, G.J., Grosse-Kunstleve, R.W.*, et al.* (2010). PHENIX: a comprehensive Python-based system for macromolecular structure solution. Acta Crystallogr D Biol Crystallogr *66*, 213-221.

Arnaout, M.A., Goodman, S.L., and Xiong, J.P. (2007). Structure and mechanics of integrin-based cell adhesion. Curr Opin Cell Biol *19*, 495-507.

Blystone, S.D., Graham, I.L., Lindberg, F.P., and Brown, E.J. (1994). Integrin alpha v beta 3 differentially regulates adhesive and phagocytic functions of the fibronectin receptor alpha 5 beta 1. J Cell Biol *127*, 1129-1137.

Brooks, B.R., Brooks, C.L., 3rd, Mackerell, A.D., Jr., Nilsson, L., Petrella, R.J., Roux, B., Won, Y., Archontis, G., Bartels, C., Boresch, S.*, et al.* (2009). CHARMM: the biomolecular simulation program. J Comput Chem *30*, 1545-1614.

Caswell, P.T., Chan, M., Lindsay, A.J., McCaffrey, M.W., Boettiger, D., and Norman, J.C. (2008). Rab-coupling protein coordinates recycling of alpha5beta1 integrin and EGFR1 to promote cell migration in 3D microenvironments. J Cell Biol *183*, 143-155.

Christoforides, C., Rainero, E., Brown, K.K., Norman, J.C., and Toker, A. (2012). PKD controls alphavbeta3 integrin recycling and tumor cell invasive migration through its substrate Rabaptin-5. Dev Cell *23*, 560-572.

Coller, B.S., and Shattil, S.J. (2008). The GPIIb/IIIa (integrin alphaIIbbeta3) odyssey: a technology-driven saga of a receptor with twists, turns, and even a bend. Blood *112*, 3011-3025.

Dumont, R.A., Hildebrandt, I., Su, H., Haubner, R., Reischl, G., Czernin, J.G., Mischel, P.S., and Weber, W.A. (2009). Noninvasive imaging of alphaVbeta3 function as a predictor of the antimigratory and antiproliferative effects of dasatinib. Cancer Res *69*, 3173-3179.

Emsley, P., and Cowtan, K. (2004). Coot: model-building tools for molecular graphics. Acta Crystallogr D Biol Crystallogr *60*, 2126-2132.

Friedland, J.C., Lee, M.H., and Boettiger, D. (2009). Mechanically activated integrin switch controls alpha5beta1 function. Science *323*, 642-644.

Hatley, R.J.D., Macdonald, S.J.F., Slack, R.J., Le, J., Ludbrook, S.B., and Lukey, P.T. (2018). An alphav-RGD Integrin Inhibitor Toolbox: Drug Discovery Insight, Challenges and Opportunities. Angew Chem Int Ed Engl *57*, 3298-3321.

Humphrey, W., Dalke, A., and Schulten, K. (1996). VMD: visual molecular dynamics. J Mol Graph *14*, 33-38, 27-38.

Kapp, T.G., Rechenmacher, F., Neubauer, S., Maltsev, O.V., Cavalcanti-Adam, E.A., Zarka, R., Reuning, U., Notni, J., Wester, H.J., Mas-Moruno, C.*, et al.* (2017). A Comprehensive Evaluation of the Activity and Selectivity Profile of Ligands for RGD-binding Integrins. Sci Rep *7*, 39805.

Kimura, R.H., Cheng, Z., Gambhir, S.S., and Cochran, J.R. (2009a). Engineered knottin peptides: a new class of agents for imaging integrin expression in living subjects. Cancer Res *69*, 2435-2442.

Kimura, R.H., Levin, A.M., Cochran, F.V., and Cochran, J.R. (2009b). Engineered cystine knot peptides that bind alphavbeta3, alphavbeta5, and alpha5beta1 integrins with low-nanomolar affinity. Proteins *77*, 359-369.

Krieger, F., Moglich, A., and Kiefhaber, T. (2005). Effect of proline and glycine residues on dynamics and barriers of loop formation in polypeptide chains. J Am Chem Soc *127*, 3346-3352.

Kwan, B.H., Zhu, E.F., Tzeng, A., Sugito, H.R., Eltahir, A.A., Ma, B., Delaney, M.K., Murphy, P.A., Kauke, M.J., Angelini, A.*, et al.* (2017). Integrin-targeted cancer immunotherapy elicits protective adaptive immune responses. J Exp Med *214*, 1679-1690.

Mason, W.P. (2015). End of the road: confounding results of the CORE trial terminate the arduous journey of cilengitide for glioblastoma. Neuro Oncol *17*, 634-635.

McCoy, A.J., Grosse-Kunstleve, R.W., Adams, P.D., Winn, M.D., Storoni, L.C., and Read, R.J. (2007). Phaser crystallographic software. J Appl Crystallogr *40*, 658-674.

Mehta, R.J., Diefenbach, B., Brown, A., Cullen, E., Jonczyk, A., Gussow, D., Luckenbach, G.A., and Goodman, S.L. (1998). Transmembrane-truncated alphavbeta3 integrin retains high affinity for ligand binding: evidence for an 'inside-out' suppressor? Biochem J *330 (Pt 2)*, 861-869.

Moore, S.J., Hayden Gephart, M.G., Bergen, J.M., Su, Y.S., Rayburn, H., Scott, M.P., and Cochran, J.R. (2013). Engineered knottin peptide enables noninvasive optical imaging of intracranial medulloblastoma. Proc Natl Acad Sci U S A *110*, 14598-14603.

Nero, T.L., Morton, C.J., Holien, J.K., Wielens, J., and Parker, M.W. (2014). Oncogenic protein interfaces: small molecules, big challenges. Nat Rev Cancer *14*, 248-262.

Otwinowski, Z., and Minor, W. (1997). Processing of X-ray diffraction data collected in oscillation mode. Methods Enzymol *276*, 307-326.

Pabon, N.A., and Camacho, C.J. (2017). Probing protein flexibility reveals a mechanism for selective promiscuity. Elife *6*.

Phillips, J.C., Braun, R., Wang, W., Gumbart, J., Tajkhorshid, E., Villa, E., Chipot, C., Skeel, R.D., Kale, L., and Schulten, K. (2005). Scalable molecular dynamics with NAMD. J Comput Chem *26*, 1781-1802.

Raab-Westphal, S., Marshall, J.F., and Goodman, S.L. (2017). Integrins as Therapeutic Targets: Successes and Cancers. Cancers (Basel) *9*.

Reynolds, A.R., Hart, I.R., Watson, A.R., Welti, J.C., Silva, R.G., Robinson, S.D., Da Violante, G., Gourlaouen, M., Salih, M., Jones, M.C.*, et al.* (2009). Stimulation of tumor growth and angiogenesis by low concentrations of RGD-mimetic integrin inhibitors. Nat Med *15*, 392-400.

Sheldrake, H.M., and Patterson, L.H. (2014). Strategies to inhibit tumor associated integrin receptors: rationale for dual and multi-antagonists. J Med Chem *57*, 6301-6315.

Takada, Y., Ye, X., and Simon, S. (2007). The integrins. Genome Biol *8*, 215.

Van Agthoven, J.F., Xiong, J.P., Alonso, J.L., Rui, X., Adair, B.D., Goodman, S.L., and Arnaout, M.A. (2014). Structural basis for pure antagonism of integrin alphaVbeta3 by a high-affinity form of fibronectin. Nat Struct Mol Biol *21*, 383-388.

Wilson, I.A., and Stanfield, R.L. (1994). Antibody-antigen interactions: new structures and new conformational changes. Curr Opin Struct Biol *4*, 857-867.

Xiong, J.P., Mahalingham, B., Alonso, J.L., Borrelli, L.A., Rui, X., Anand, S., Hyman, B.T., Rysiok, T., Muller-Pompalla, D., Goodman, S.L.*, et al.* (2009). Crystal structure of the complete integrin alphaVbeta3 ectodomain plus an alpha/beta transmembrane fragment. J Cell Biol *186*, 589-600.

Xiong, J.P., Stehle, T., Diefenbach, B., Zhang, R., Dunker, R., Scott, D.L., Joachimiak, A., Goodman, S.L., and Arnaout, M.A. (2001). Crystal structure of the extracellular segment of integrin alpha Vbeta3. Science *294*, 339-345.

Xiong, J.P., Stehle, T., Zhang, R., Joachimiak, A., Frech, M., Goodman, S.L., and Arnaout, M.A. (2002). Crystal structure of the extracellular segment of integrin alpha Vbeta3 in complex with an Arg-Gly-Asp ligand. Science *296*, 151-155.

Figure Legends

A.

```
EETI-II  GCP-----RILMRCKQDSDCLAGCVCGPNGFCG
2.5D     GCPQGRGDWAPTSCKQDSDCLAGCVCGPNGFCG
2.5F     GCPRPRGDNPPLTCKQDSDCLAGCVCGPNGFCG
```

B.

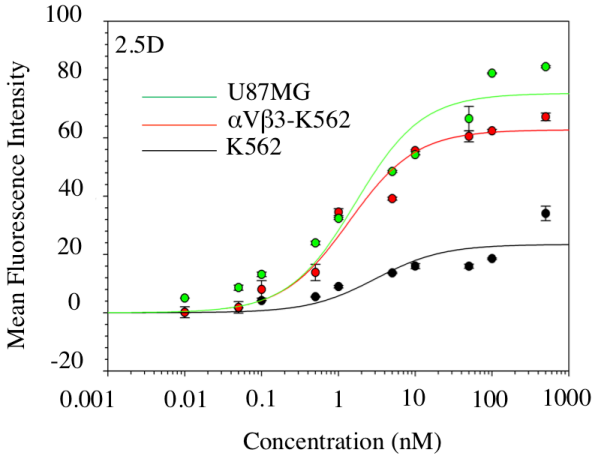

C.

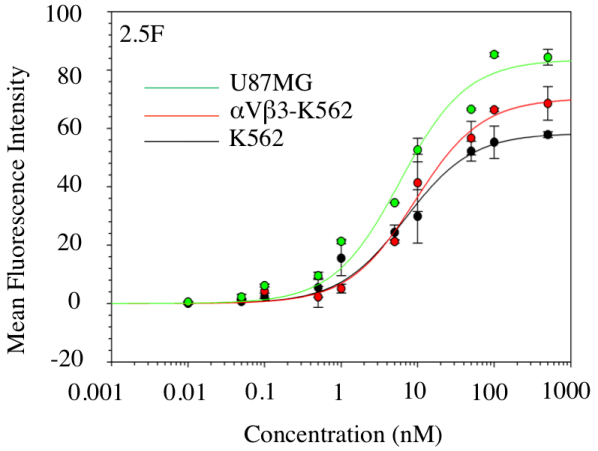

D.

Ligand	K562	αVβ3-K562	U87MG
2.5D	Not measured	1.4 (±0.4) nM	1.7 (±0.6) nM
2.5F	6.9 (±1.3) nM	9.2 (±1.4) nM	5.9 (±1.3) nM

Figure 1. Primary sequence and binding properties of knottins 2.5D and 2.5F. (A) The primary structure of EETI-II and the engineered knottins 2.5D and 2.5F, where the 6-residue trypsin-binding loop in native knottin is replaced with an 11-residue loop (amino acids 2-12) containing the RGD motif. (B, C) Dose-response curves showing binding of Fc fusions of 2.5D (B) and 2.5F (C) to native integrins expressed on U87MG (green), αVβ3 expressed on transfected K562 cells (αVβ3-K562, red), and native α5β1 on K562 cells (black). (D) Average equilibrium binding constant (K_D) values from the binding data shown in B, C, with error representing standard deviation of triplicate experiments.

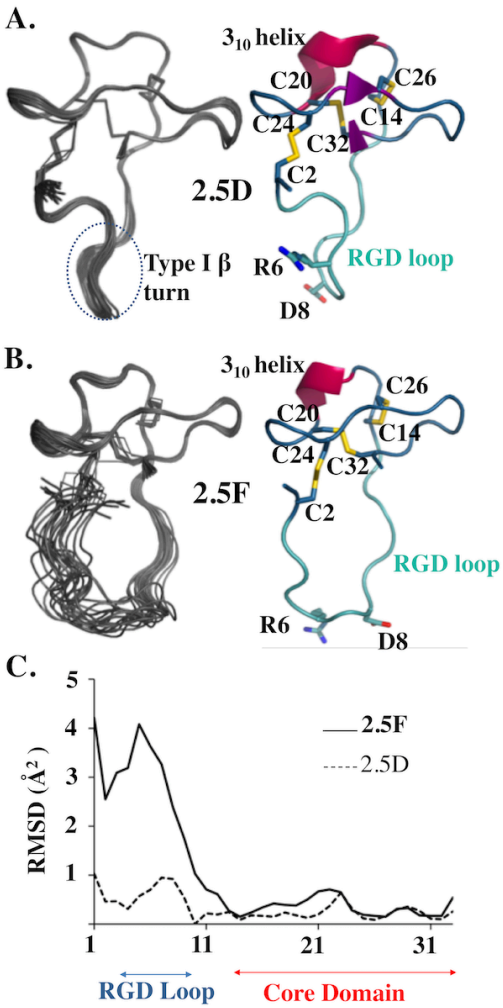

D.

Ligand	RMSD RGD loop (4-10)	RMSD Core domain (14-33)	RMSD Overall
2.5F	2.76 Å² (±1.00)	0.35 Å² (±0.18)	1.14 Å² (±1.29)
2.5D	0.67 Å² (±0.22)	0.22 Å² (±0.12)	0.35 Å² (±0.26)

Figure 2. NMR structures and analysis of 2.5D and 2.5F. (A, B) Solution NMR structures of knottins 2.5D (A) and 2.5F (B) represented as the 20 lowest energy conformers. Ribbon diagrams of the lowest energy conformer of 2.5D and 2.5F are shown to the right. The RGD loop is in cyan with the integrin RGD binding sequence in sticks. The core domain is blue with disulfide bonds in yellow sticks. The 3_{10} helix is represented in red cartoon. (C) RMSD of solution structure of 2.5D and 2.5F plotted versus residue number. The RGD loop (residue 4-10) and core domain (residue 14-33) are indicated. (D) Table summarizing the RMSD values per domain shown as mean±S.D.: core domain (residue 14-33) and RGD loop (residue 4-10).

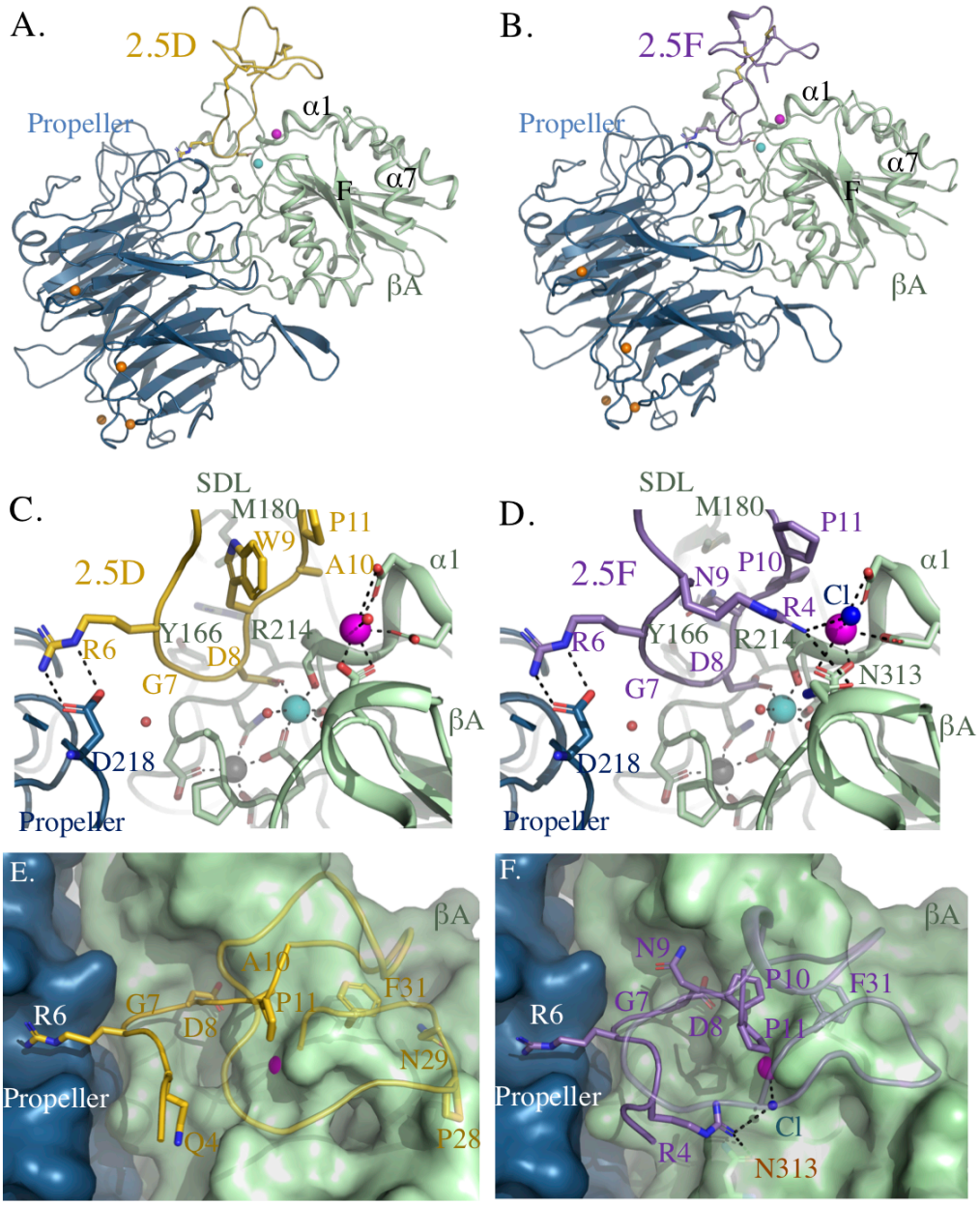

Figure 3. Crystal structures of αVβ3 bound to 2.5D or 2.5F. (A, B) Ribbon diagrams of αVβ3 head bound to 2.5D (yellow, A) and 2.5F (purple, B). The propeller is in blue and βA domain green. Mn^{2+} ions at LIMBS (gray), MIDAS (cyan) and ADMIDAS (magenta) are shown as spheres (also in C-F). (C, D) Ribbon diagrams showing key electrostatic and hydrogen bond interactions and metal ion coordination in the structure of αVβ3/2.5D (C) and αVβ3/2.5F (D). 2.5F-Arg^{4} hydrogen bonds with β3-Asn^{313}. Additionally, 2.5F contacts the ADMIDAS ion colored in purple through a chloride (Cl) ion represented as a blue sphere. Water molecules are shown as small red spheres. (E, F) Integrin-binding pocket for 2.5D and 2.5F. αVβ3 is shown as solvent accessible surface areas, with the 2.5D and 2.5F shown in cartoon. Contact residues are shown in sticks and includes residues with van der Waals (≤4Å) contact to β3: Pro^{11}, Phe^{31}, Asn^{29}, and ion Pro^{29} for 2.5D; Asn^{9}, Pro^{10}, Pro^{11} and Phe^{31} for 2.5F.

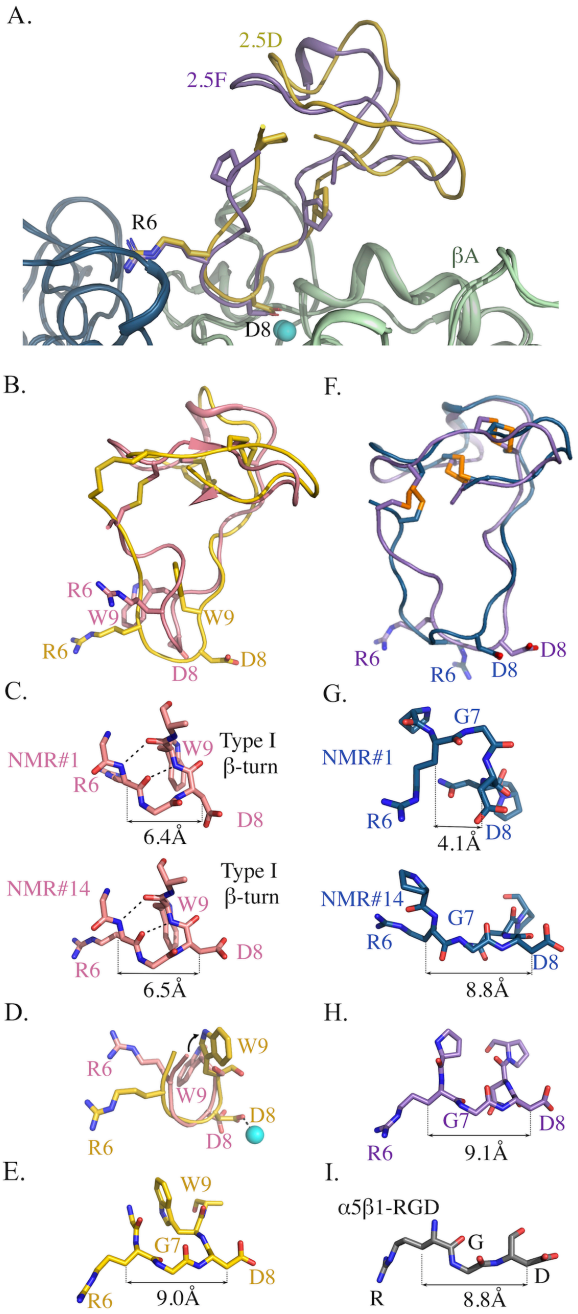

Figure 4. Structural comparisons of 2.5D and 2.5F in solution and integrin bound. (A) Ribbon diagram of the superposed crystal structures of 2.5D (yellow) and 2.5F (purple) in the integrin bound state. (B) Crystal structures of 2.5D (yellow) and 2.5F (purple) superimposed on lowest energy model of unbound NMR 2.5D structure (B, rose) and (F, dark blue). (C, G) Stick diagrams of the RGD loop in apo 2.5D (pink) and apo 2.5F (dark blue) of lowest energy model #1 and #14 of each. The apo structures show a β hairpin Type I turn in the RGD loop of the solution structure of 2.5D. (D) Superposition of GRGDW (residues 5-9) in the main chain of

NMR model #1 of apo 2.5D (rose) and its crystal structure (yellow) in complex with the integrin. The black arrow shows the conformational change of W9 from pointing outwards towards solvent to inwards in the RGD loop structure. (E, H) Crystal structures of the integrin-bound RGD loops of 2.5D (E) and 2.5F (H). (I) Stick diagram of RGD loop in RGD-ligated α5β1 (PDB code 4WK4). The Cβ-Cβ distances between R6 and D8 in C, G, H, E and I are shown.

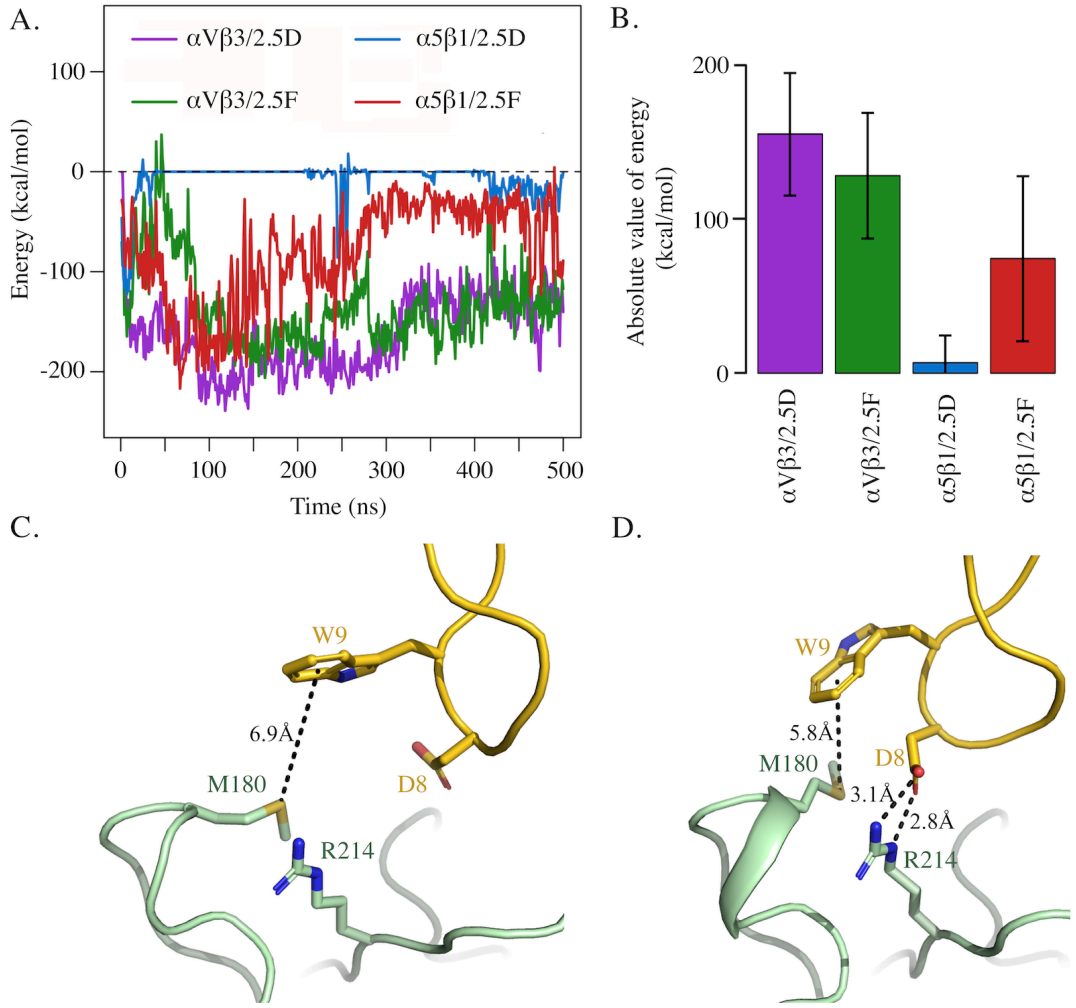

Figure 5. MD simulations of 2.5D/2.5F binding to αVβ3/α5β1. Knottin variants were initially separated by 9Å. (A) Energy over time and (B) bar graph (mean± SE) showing absolute value of binding energies between 2.5d/2.5F and αVβ3/α5β1 averaged over 500ns of simulation time. Differences among the groups are significant at $p<2.2e^{-16}$. (C, D) Selected residues in the αVβ3 structure binding to 2.5D at t=0.220 ns and t=0.960 ns of MD simulation. The interaction between W^9 and M^{180} (dotted lines) positioned D^8 in closer proximity of R^{214} to form a salt bridge.

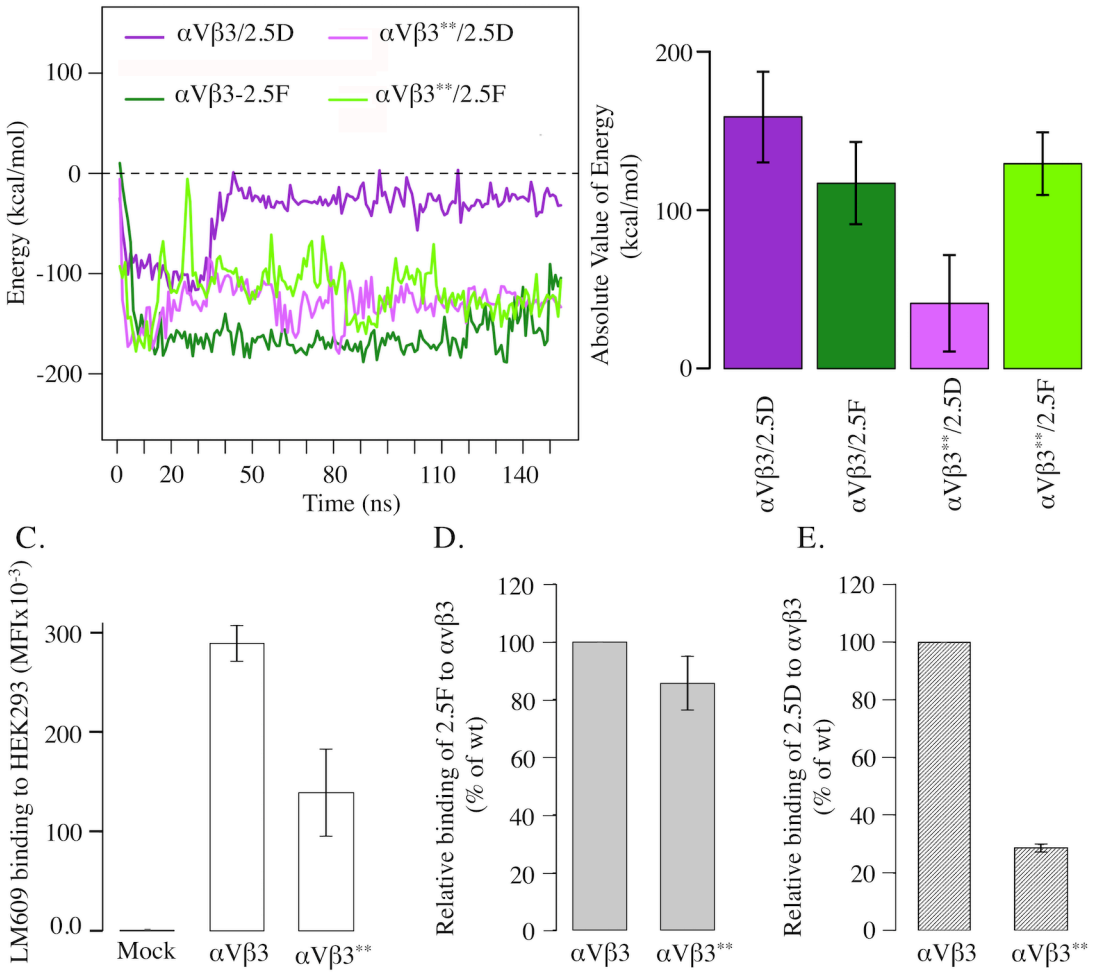

Figure 6. Binding of 2.5D/2.5F to αVβ3 and α5β1. (A,B) MD simulations of 2.5D and 2.5F binding to integrins. (A) Energy over time and (B) absolute value of energies (histograms (mean ± SD) for 160 ns of 2.5D/2.5F binding to wild type αVβ3 and αVβ3** double mutant β3-M180A and β3-R214G simulations. Differences among the groups are significant at $p<2.2e^{-16}$ except for the difference between αVβ3/2.5F and αVβ3**/2.5F where the p value is $1.892e^{-06}$. (C-E) Histograms (mean ± SE, n=4 independent experiments) showing binding of integrin antibody or Alexa 647-labeled 2.5F or 2.5D (each at 65 nM) to transiently transfected HEK293T-$\alpha_V\beta_3$ and double mutant β3-M180A and β3-R214G αVβ3** in 1 mM Ca^{2+}/Mg^{2+} as determined by FACS analysis. (C) Binding of αVβ3 heterodimer specific antibody LM609 detected by APC-labeled goat anti-mouse Fc-specific antibody. (D) Binding of Alexa647-2.5F to αVβ3 and αVβ3**. (E) Binding of Alexa647-2.5D to αVβ3 and αVβ3**. Binding of the knottin to wild-type αVβ3 in D and E was set to 100%.

Supplementary Material

Table S1. NMR structural statistics for 2.5D and 2.5F 20-conformer ensembles

	2.5D	**2.5F**
PDB Code	2M7T	6MM4
NMR-derived restraints		
Interproton total	462	340
short-range, |i-j|<=1	248	223
medium-range, 1<|i-j|<5	78	48
long-range, |i-j|>=5	136	69
Dihedral angles	32	35
Hydrogen bonds	16	16
Disulfide bonds	18	18
Ramachandran statistics		
Residues in		
most favored regions (%)	86.3	87.5
additional allowed regions (%)	13.7	11.4
generously allowed regions (%)	0.0	0.5
disallowed regions (%)	0.0	0.7
RMSD statistics (residues 1-33)		
Average backbone RMSD to mean (Å)	0.26 +/- 0.06	1.04 +/- 0.28
Average heavy atom RMSD to mean (Å)	0.48 +/- 0.09	1.52 +/- 0.3

Table S2. Data collection and refinement statistics.

Data collection	**αVβ3/2.5D**	**αVβ3/2.5F**
PDB Code	6MSL	6MSU
Beamline	ID19 at APS	ID19 at APS
Space group	$P3_221$	$P3_221$
Unit cell dimensions (Å, °)	*a*=*b*=129.8, *c*=305.9; α=β=90, γ=120	*a*=*b*=129.9, *c*=305.9; α=β=90, γ=120
Resolution range (Å)	50.0-3.1	50.0-3.1
Wavelength (Å)	0.97921	0.97921
Total reflections	1,919,957	945,125
Unique reflections	54,885 (5,389)*	54,732 (5,385)
Completeness	100 (100)	100 (100)
Redundancy	6.9 (7.0)	6.2 (6.3)
Molecules in asymmetric unit	1	1
Average I/σ	14.1 (1.7)	15.3 (2.0)
R_{merge} (%)	14.9 (100)	12.7 (100)
R_{meas} (%)	16.2 (100)	13.9 (100)
R_{sym} (%)	6.2 (68.6)	5.5 (57.1)
Wilson *B*-factor	65.6	62.7
Refinement statistics		
Resolution range (Å)	49.2-3.1	49.3-3.1
R_{factor} (%)	24.0 (32.4)	23.4 (32.0)
R_{free} (%)#	26.6 (29.2)	26.3 (31.6)
No. of atoms	13,132	13,158
Protein	12,713	12,714
Water	4	4
Mn^{2+}	8	8
Glc-NAc	407	431
Chloride	0	1
Average *B*-factor for all atoms (Å^2)	62.3	61.4
r.m.s. deviations		
Bond lengths (Å)	0.005	0.005
Bond angles (°)	1.11	1.11
Ramachandran plot		
Most favored (%)	89.8	91.3
Allowed regions (%)	9.5	8.4
Outliers (%)	0.7	0.3
Clashscore (%)	6.0	5.7
Rotamer outliers (%)	2.5	2.5

* Values in parentheses are for the highest resolution shell (0.1Å)
# R_{free} was calculated with 5% of the data

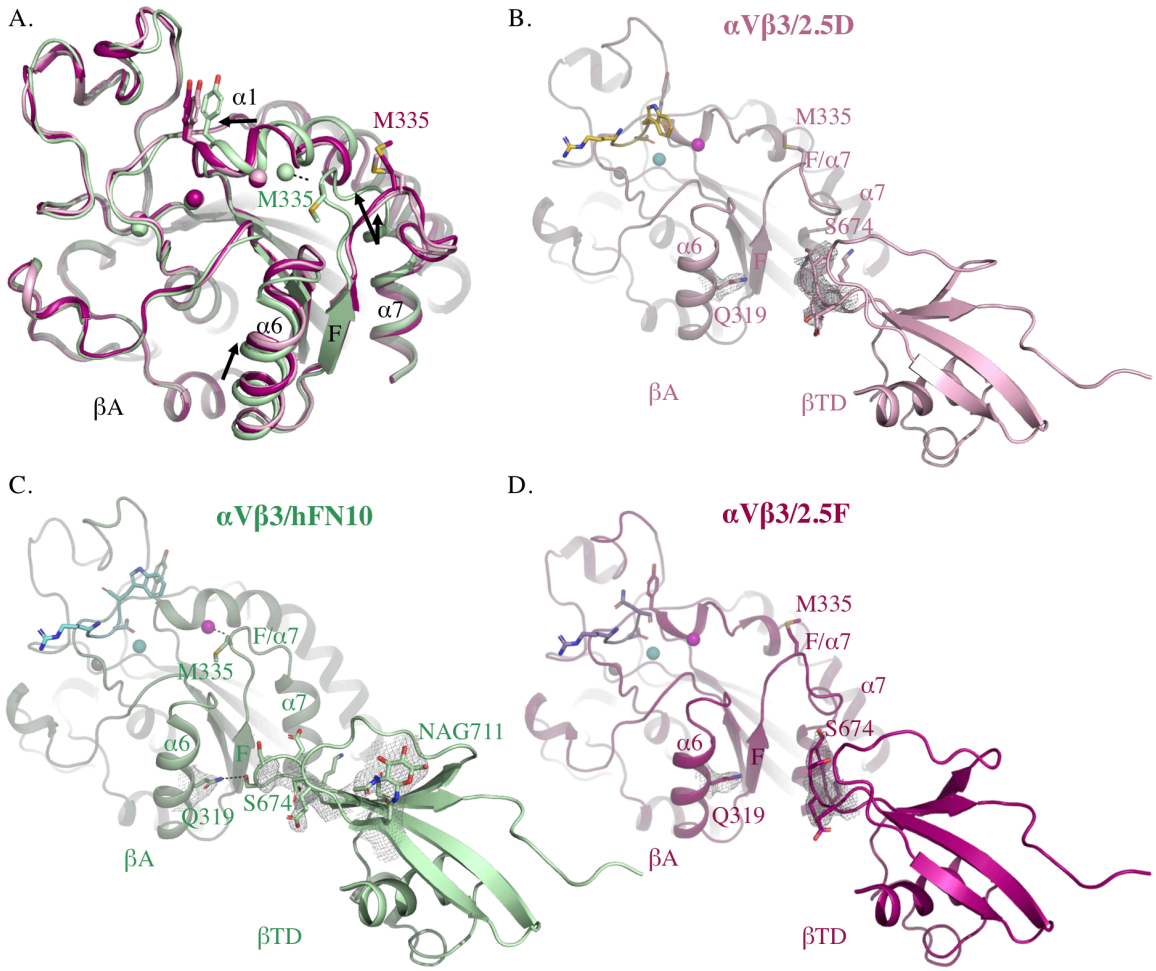

Figure S1: **Conformational changes and βA/β-tail interface in crystal structures of αVβ3 in complex with 2.5D, 2.5F or hFN10.** A) Superimposition of βA domains of $\alpha_V\beta_3$ bound to hFN10 (green), 2.5F (dark pink) and 2.5D (pink) shown in cartoon. Blue arrows show the inward movement of βA-α1 towards MIDAS and translation of α6 between αVβ3/hFN10 (inactive) and αVβ3/2.5F or αVβ3/2.5D (active). LIMBS, MIDAS and ADMIDAS are shown in spheres. (B,C,D) Cartoon diagram of βa and β-tail domains for αVβ3/2.5D (B), -hFN10 (C), and -2.5F (D). RGD loop is shown in gold (2.5D), light blue (hFN10) and purple (2.5D). 2Fobs − Fcalc maps at 1.0 σ for β-tail residues 671-676 of βA and βA-Gln^{319} in αVβ3/2.5D (B), αVβ3/hFN10 (C) αVβ3/2.5F (D). NAG711 is shown in stick in αVβ3/hFN10 but not in αVβ3/2.5D/2.5F. RGDW of 2.5D and hFN10, RGDN of 2.5F are respectively shown yellow, light blue and purple sticks. LIMBS, MIDAS and ADMIDAS are shown in respectively grey, cyan and magenta spheres.